









Half-integer Shapiro steps in highly transmissive InSb nanoflag Josephson junctions

A. Iorio ^{1,*}, A. Crippa ¹, B. Turini ^{1,†}, S. Salimian,¹ M. Carrega,² L. Chiroli ¹, V. Zannier ¹, L. Sorba ¹,
E. Strambini ¹, F. Giazotto,¹ and S. Heun ^{1,‡}

¹NEST, Istituto Nanoscienze-CNR and Scuola Normale Superiore, Piazza San Silvestro 12, 56127 Pisa, Italy

²CNR-SPIN, Via Dodecaneso 33, 16146 Genoa, Italy



(Received 30 March 2023; revised 26 May 2023; accepted 6 June 2023; published 7 July 2023)

We investigate a ballistic InSb nanoflag-based Josephson junction with Nb superconducting contacts. The high transparency of the superconductor-semiconductor interfaces enables the exploration of quantum transport with parallel short and long conducting channels. Under microwave irradiation, we observe half-integer Shapiro steps that are robust to temperature, suggesting their possible nonequilibrium origin. Our results demonstrate the potential of ballistic InSb nanoflags Josephson junctions as a valuable platform for understanding the physics of hybrid devices and investigating their nonequilibrium dynamics.

DOI: [10.1103/PhysRevResearch.5.033015](https://doi.org/10.1103/PhysRevResearch.5.033015)

Advancing quantum technologies have made the investigation of low-dimensional hybrid superconducting nanostructures a major area of research in recent years. When a normal conductor is coupled to a superconductor, the superconducting correlations can penetrate into the nonsuperconducting region through the proximity effect [1,2]. As a result, the hybrid system can exhibit unique properties derived from both the normal and superconducting components, offering exciting possibilities for novel functionalities. This phenomenon has been investigated in various solid-state platforms, including semiconductors [3,4], two-dimensional electron systems [5–7], magnetic and ferroelectric materials [8,9], and topological insulators [10–12]. In this context, indium antimonide (InSb) is a particularly promising semiconductor, known for its high electron mobility, narrow bandgap, strong Rashba spin-orbit coupling, and large g^* factor [7,13–16]. Due to the challenges of growing InSb quantum wells on insulating substrates, free-standing InSb nanoflags have emerged as a highly flexible platform, as they can be grown without defects on lattice-mismatched substrates [17–28]. They have also been referred to as nanoflakes, nanosheets, or nanosails in the literature [18–20,29]. Recently InSb nanoflags have been used to realize proximity-induced superconductor-normal conductor-superconductor (SNS) Josephson junctions, which exhibit ballistic and gate-tunable supercurrents [21,30,31], clear subharmonic gap structures [22,30], and nonlocal and

nonreciprocal supercurrent transport [19,31]. These developments highlight the potential of InSb nanoflags as a platform for exploring the complex dynamics between charge, spin, and superconducting correlations, including topological superconductivity [32,33], gate-tunable hybrid superconducting qubits [34–36], and nonequilibrium quasiparticle dynamics [36–38].

In this work we present a thorough investigation of highly transmissive ballistic Josephson junctions on InSb nanoflags made with niobium (Nb) contacts. Compared to previous works [30,31], our device has a higher junction transparency, which enables the investigation of unexplored transport regimes. Our findings reveal the coexistence of parallel short and long conducting channels, as confirmed by the temperature dependence of the critical current and magnetoresistance. Under microwave irradiation, we observe Shapiro steps at half-integer values of the canonical voltage $hf/2e$, which exhibit a nonmonotonic evolution with temperature. The observation suggests that a nonequilibrium state is formed in the junction due to the microwave drive.

The device depicted in Figs. 1(a) and 1(b) consists of a planar SNS junction made of an InSb nanoflag with two Nb contacts. Previous studies have revealed that these InSb nanoflags are defect-free and exhibit a zincblende structure with high mobility (up to $29\,500\text{ cm}^2\text{V}^{-1}\text{s}^{-1}$) and a mean-free path $l_e \simeq 500\text{ nm}$ at 4.2 K [28]. The Fermi wavelength $\lambda_F \simeq 30\text{ nm}$ for a carrier concentration of $n_s \simeq 8.5 \times 10^{11}\text{ cm}^{-2}$ is comparable to the thickness of the nanoflags ($\simeq 100\text{ nm}$), resulting in a strong quasi-two-dimensional character. Measurements were performed using a standard four-wire technique at the base temperature of $T = 75\text{ mK}$ of a dilution refrigerator. A highly doped Si backgate allows for control of the carrier density of the InSb and was set to $V_G = 40\text{ V}$ for the results shown in the following. Microwave signals are applied via an open-ended attenuated coaxial cable placed $\sim 1\text{ cm}$ away from the chip surface. The junction dynamics is modeled using an extended resistively and capacitively shunted junction (RCSJ) model, which takes into account the dissipative environment surrounding the junction, as depicted in Fig. 1(c) [3,40,41]. Further information on materials,

*andrea.iorio@sns.it

†Present address: ICFO - Institut De Ciències Fòtoniques, The Barcelona Institute of Science and Technology, 08860 Castelldefels (Barcelona), Spain.

‡stefan.heun@nano.cnr.it

Published by the American Physical Society under the terms of the [Creative Commons Attribution 4.0 International license](https://creativecommons.org/licenses/by/4.0/). Further distribution of this work must maintain attribution to the author(s) and the published article's title, journal citation, and DOI.

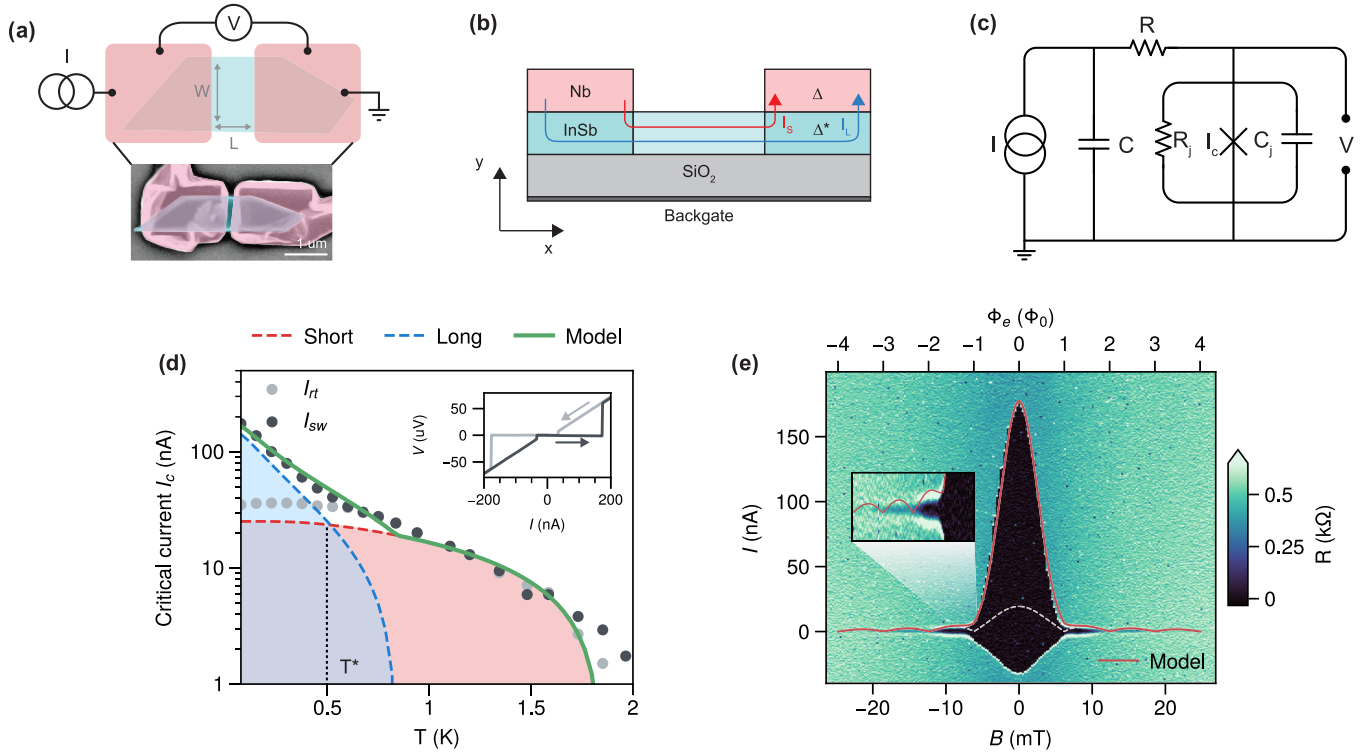


FIG. 1. (a) Upper part: sketch of the sample with the relevant dimensions and a simplified measurement setup. The junction length is $L = 80$ nm and the width is $W = 650$ nm. Lower part: scanning electron micrograph of the SNS junction. The InSb nanoflag has a trapezoidal shape, and the Nb contacts are patterned on top of it. (b) Schematic cross section of the device, where the superconducting Nb contacts with gap Δ proximitize an induced gap Δ^* in the InSb layer [39]. The red and blue lines represent, respectively, the short and long conducting channels that are discussed in (d). (c) Extended RCSJ model, with the Josephson junction of critical current I_c in parallel with a shunt resistance R_j and capacitance C_j . Additional shunt capacitance C and resistor R take into account the dissipative environment around the junction. (d) Temperature dependence of the switching current I_{sw} (black dots) and the retrapping current I_r (gray dots). The blue and red areas indicate the contributions of the long and short conducting channels, respectively, as estimated from the corresponding models. The green line represents the sum of the two contributions. Inset: forward (black line) and backward (gray line) current sweeps used to extract the switching I_{sw} and retrapping I_r currents, respectively. (e) Differential resistance $R = dV/dI$ plotted as a function of the bias current I and the out-of-plane magnetic field B . The red curve takes into account both the long and short model contributions. The gray line shows the Fraunhofer pattern resulting from the short channel only. The inset provides a zoomed-in view of lobes in the low-bias region.

fabrication, and measurement techniques can be found in Appendix A.

We first characterize the device in the absence of microwave irradiation. A typical back and forth sweep $V(I)$ is presented in the inset of Fig. 1(d), in which a current bias I is applied and the resulting voltage drop V across the junction is measured. The $V(I)$ characteristic shows a considerable hysteresis with a switching current $I_{sw} \simeq 170$ nA and a retrapping current $I_r \simeq 30$ nA. The hysteresis in planar SNS junctions is commonly due to electronic heating in the normal region [42], with a finite junction capacitance C_j potentially contributing [43]. Additional contributions to the hysteresis can arise from the cross-capacitance of the bonding pads via the backgate electrode, resulting in the underdamping of the junction [44,45].

Figure 1(d) shows the temperature dependence of the switching and retrapping currents on a semilog scale. We can distinguish two distinct regions in the data. For temperatures $T > T^*$, with $T^* \sim 500$ mK [see Fig. 1(d)], the switching current follows the predictions of a short junction model (shown as a red shaded area). However, for $T \leq T^*$, we see a

deviation from the short junction behavior, and the switching current follows an exponential increase with decreasing T , which is characteristic of long junctions (blue shaded area). The data can be well reproduced over the entire temperature range using a simple model that considers the transport predominantly determined by two conducting channels, long and short, as illustrated in Fig. 1(b) and demonstrated by the green line in Fig. 1(d). The coincidence of the separation of switching and retrapping currents occurring approximately at T^* is purely coincidental.

In the short junction limit $L \ll \xi_N$ (where $\xi_N = \hbar v_F / \Delta \simeq 720$ nm is the coherence length, with $v_F \simeq 1.5 \times 10^6$ m/s [28] and $\Delta = 1.764 k_B T_c \simeq 1.35$ meV, with $T_c \simeq 8.9$ K being the Nb critical temperature), the supercurrent flows directly through the InSb region between the Nb contacts separated by $L = 80$ nm. For simplicity, we assume that all modes in the junction have equal effective transmission τ , which can be described in the ballistic limit ($L \ll l_e$) by [46]

$$I_S(T) = \max_{\varphi} \frac{\bar{N} e \Delta^{*2}(T)}{2\hbar} \frac{\tau \sin \varphi}{E_A(\varphi, T)} \tanh \frac{E_A(\varphi, T)}{2k_B T}, \quad (1)$$

with \bar{N} the number of effective modes, $E_A(\varphi, T) = \Delta^*(T)\sqrt{1 - \tau \sin^2(\varphi/2)}$ the Andreev bound state (ABS) energy of the mode, $\Delta^*(T) = \Delta^* \tanh(1.74\sqrt{T_c^*/T} - 1)$ the temperature-dependent induced energy gap [47], and φ the macroscopic phase difference across the junction. The best fit with the short junction model yields the red dashed line in Fig. 1(d), with a single mode $\bar{N} = 1$, $\tau \simeq 0.93$, and $T_c^* \simeq 1.85$ K ($\Delta^* \simeq 280$ μeV), and a value of critical current $I_S \simeq 25$ nA at $T = 75$ mK. The observed lower values of currents are consistent with the transport mechanism illustrated in Fig. 1(b), where the supercurrent flows between the two proximized InSb regions with an induced gap Δ^* , rather than being dominated by the Nb gap Δ .

The exponentially enhanced conduction at low temperatures is typical of long channel states (of length d). The conduction via these states holds in the long junction limit $d \gg \xi_N$ and reads [48]:

$$I_L(T) = \frac{E_{Th}}{R_N e} a \left[1 - 1.3 \exp\left(-\frac{aE_{Th}}{3.2k_B T}\right) \right], \quad (2)$$

where $E_{Th} = \hbar v_F l_e / 2d^2$ is the Thouless energy [2], R_N is the junction resistance and $a = 3$ [49]. The best fit of the long junction model is shown as the blue dashed line in Fig. 1(d) and yields $E_{Th} \simeq 20$ μeV , corresponding to $d \simeq 3.5$ μm , close to the total length of the InSb nanoflag (3.35 μm), $R_N \simeq 400$ Ω and a critical current $I_L \simeq 140$ nA at $T = 75$ mK.

Previous studies have documented similar results in highly transmissive ballistic SNS junctions with topological insulators or graphene [4,45,50–54], with the behavior being attributed to contributions from both surface and bulk states [51,53]. One study linked the low-temperature enhancement to a low-energy Andreev bound state localized around the circumference of the junction [50]. In our nanoflags, this could be consistent with electronic transport at the edges of the nanoflag due to band bending, similarly to what has been reported by de Vries *et al.* [19]. Compared to earlier works on InSb nanoflags that employed a Ti sticking layer between Nb and InSb [30,31], the increase of I_{sw} at low temperature is consistent with the increased transparency achieved in this study through the direct deposition of bare Nb on the passivated surface of InSb, without the use of additional metallic layers.

Magnetotransport measurements further confirm the coexistence and magnitude of the two current conducting channels in the junction, providing additional insight into the current density distribution across the channels. The differential resistance of the junction $R = dV/dI$ as a function of magnetic flux is presented in Fig. 1(e). An unconventional Fraunhofer pattern, with a first lobe much more pronounced than the side lobes, is visible and well described by the superposition of a conventional Fraunhofer pattern typical of short junctions, and a monotonic quasi-Gaussian decay, which is characteristic of long SNS junctions [52,55–59]. The forward biasing of the current results in a nonsymmetrical supercurrent region for switching and retrapping currents (black area). The periodicity of the Fraunhofer pattern corresponds to one flux quantum inside the junction, taking into account a London penetration depth of $\lambda_L \simeq 100$ nm [60] and a flux enhancement of a factor of $\Gamma_f \sim 1.8$ due to flux focusing within the planar

geometry. The critical current values from short and long transport channels estimated in Fig. 1(d) are used here to model the magnetic interference patterns. The red line in Fig. 1(e) shows the combined contribution of both channels to the supercurrent $I(\Phi_e) = I_S(\Phi_e) + I_L(\Phi_e)$, where $\Phi_e = \Gamma_f B(L + 2\lambda_L)W$ is the applied magnetic flux on the uncovered junction area, with $W = 650$ nm the junction width. The standard Fraunhofer pattern $I_S(\Phi_e) = I_S |\sin[\pi(\Phi_e/\Phi_0)]/(\pi\Phi_e/\Phi_0)|$ expected for a wide-short junction and a Gaussian decay $I_L(\Phi_e) = I_L \exp(-\sigma\Phi_e^2/\Phi_0^2)$, typical of a narrow-long junction, are accounted for in the calculation. We have included a possible different effective area of the long junction directly in the estimated value of $\sigma \sim 0.329$ while preserving the same flux dependence.

Our conclusions are further supported by the temperature-dependent change in the magnetoresistance, which exhibits an exponential reduction of the Gaussian component and limited variation in the Fraunhofer lobes up to $T = 800$ mK (refer to Fig. 6 in Appendix C). This further excludes the hypothesis that nonuniformity in the current distribution within the short exposed junction area, though possible in our device, is the cause of the anomalous interference pattern, as it would imply a simultaneous decrease in both the central and side lobes with temperature. The lack of distinct oscillations in the magnetoresistance indicates that possible edge states are not interfering coherently with magnetic fields perpendicular to the nanoflag. However, the impact of flux screening, phase decoherence, and transport along various facets of the flag makes it challenging to arrive at more definitive conclusions.

Having established the response of the junction at equilibrium, we will now examine how the system behaves when subjected to a microwave irradiation. In Fig. 2(a) we present a sample $V(I)$ curve with a microwave tone at frequency $f = 1.75$ GHz and applied power $P_{RF} = 12$ dBm. As it can be difficult to estimate the precise power delivered to the sample, we will refer only to the power provided by the signal generator in the following discussion. Quantized voltage steps of amplitude $n \times hf/2e$ appear in the $V(I)$ characteristic (black line), as a result of the phase locking between the microwave frequency and the junction Josephson frequency [61]. In addition to integer steps occurring at $n = \pm 1, \pm 2, \pm 3, \dots$, half-integer steps appear with $n = \pm 1/2, \pm 3/2, \pm 5/2, \dots$. The overlapping gray trace displays dV/dI and shows peaks associated to both integer and half-integer steps, some of which are highlighted by red arrows. Steps with fractions different from multiples of $1/2$ are not observed. A histogram, resulting from the binning of the voltage data, is shown on the left and provides an immediate visual representation of the length of each step. The bin unit equals the current step size, such that the number of counts corresponds to the width of the voltage plateaus.

Figure 2(b) shows a color plot of R as a function of I and P_{RF} . Sharp jumps in voltage appear as bright peaks in R , while voltage plateaus correspond to dark regions. The pattern of bright peak pairs in the data provides stark evidence of fractional steps that occur over a wide range of power and frequencies, as demonstrated by the maps at $f = 1.50$ GHz and $f = 2.00$ GHz. The region between the plateaus ± 1 displays bistability at around $P_{RF} = 10$ dBm of applied power, with sudden switching occurring between the two

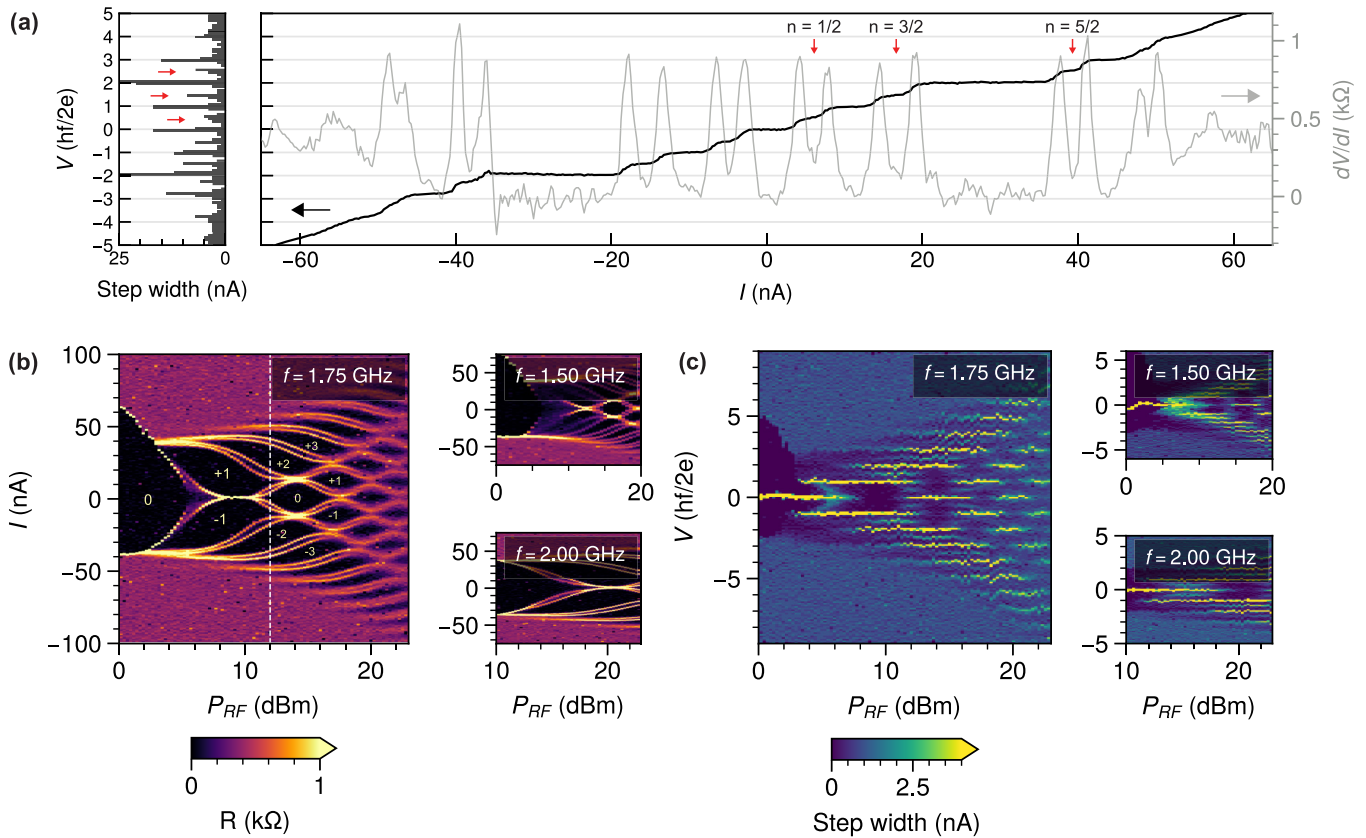


FIG. 2. (a) Sample $V(I)$ curve (black) in the presence of microwave irradiation at $P_{RF} = 12$ dBm and frequency $f = 1.75$ GHz. The gray line represents the differential resistance $R = dV/dI$ with arrows highlighting half-integer Shapiro steps. The histogram on the left shows the distribution of the voltage data. The bin unit is equal to the current step size, such that the number of counts corresponds to the width of the voltage plateaus. The value of P_{RF} refers to the one provided by the signal generator. (b) Full evolution of R as a function of current bias I and microwave power P_{RF} at $f = 1.75$ GHz. Pairs of bright peaks indicate the presence of half-integer steps. The white dashed line corresponds to the data shown in (a). Label numbers refer to the corresponding step index n . The right side shows the colormaps for $f = 1.50$ GHz and $f = 2.00$ GHz. (c) Histograms, as shown in (a), are displayed based on the data in (b) in a colorplot as a function of microwave power P_{RF} .

overlapping plateaus (see Appendix F for additional discussion). Figure 2(c) better highlights the emergence of Shapiro steps by depicting the evolution of the histogram data as a function of microwave power for various frequencies. In the Appendixes D and E, we present additional measurements for different backgate voltages, magnetic field values, and temperatures. These measurements confirm the robustness of the observed half-integer steps, indicating that the effect is not related to variations in current density or flux motion.

We then study the behavior of the system by increasing the temperature. Figure 3(a) displays Shapiro maps at temperatures ranging from $T = 75$ mK ($\sim 0.02 \Delta^*/k_B$) to $T = 1.5$ K ($\sim 0.5 \Delta^*/k_B$). The temperature rise leads to a decrease of the supercurrent and an increase in thermal fluctuations, resulting in rounded voltage plateaus. However, the half-integer steps remain stable from base temperature up to around 1 K ($\sim 0.3 \Delta^*/k_B$), where the current-phase relationship (CPR) given by the equilibrium supercurrent is expected to be mostly sinusoidal (as illustrated in Fig. 13 in Appendix H).

Figure 3(b) shows the change in step width for the steps $n = 0$ and $n = 1/2$ extracted from Fig. 3(a). The amplitude of the integer step decreases monotonically with increasing temperature, while the half-integer step shows a nonmonotonic trend, with a maximum at $T \simeq 400$ mK $\sim 0.12 \Delta^*/k_B$. This

is also demonstrated in Fig. 3(c), where the step widths for $n = 0, 1$ and $n = 1/2, 3/2$ are plotted on a semilog scale as a function of T . While the integer steps show an exponential decrease, the width of the half-integer steps first increases, then decreases, and eventually saturates due to the noise level at high temperatures. This remarkable evolution points to a nonequilibrium origin of the half-integer steps, where the supercurrent is altered by a nonequilibrium population of the ABSs that is induced by the microwave drive. This is consistent with theoretical predictions and experimental observations that nonequilibrium supercurrents are less sensitive to temperature compared to equilibrium supercurrents, which are exponentially suppressed [5,62–66].

In Appendix G we provide data from an additional device with lower transparency. While the junction behaves similarly under microwave irradiation, the signatures of the half-integer steps are considerably weaker.

Despite their frequent occurrence, the origin of fractional steps in superconducting devices is not univocal. Measurements of fractional Shapiro step are commonly used to identify nonsinusoidal CPRs in highly transparent SNS junctions [67] or in junctions incorporating ferromagnetic layers [8,9,68,69] or those exhibiting exotic superconducting states [70,71]. Geometric or intrinsic capacitance [57,72–75] and

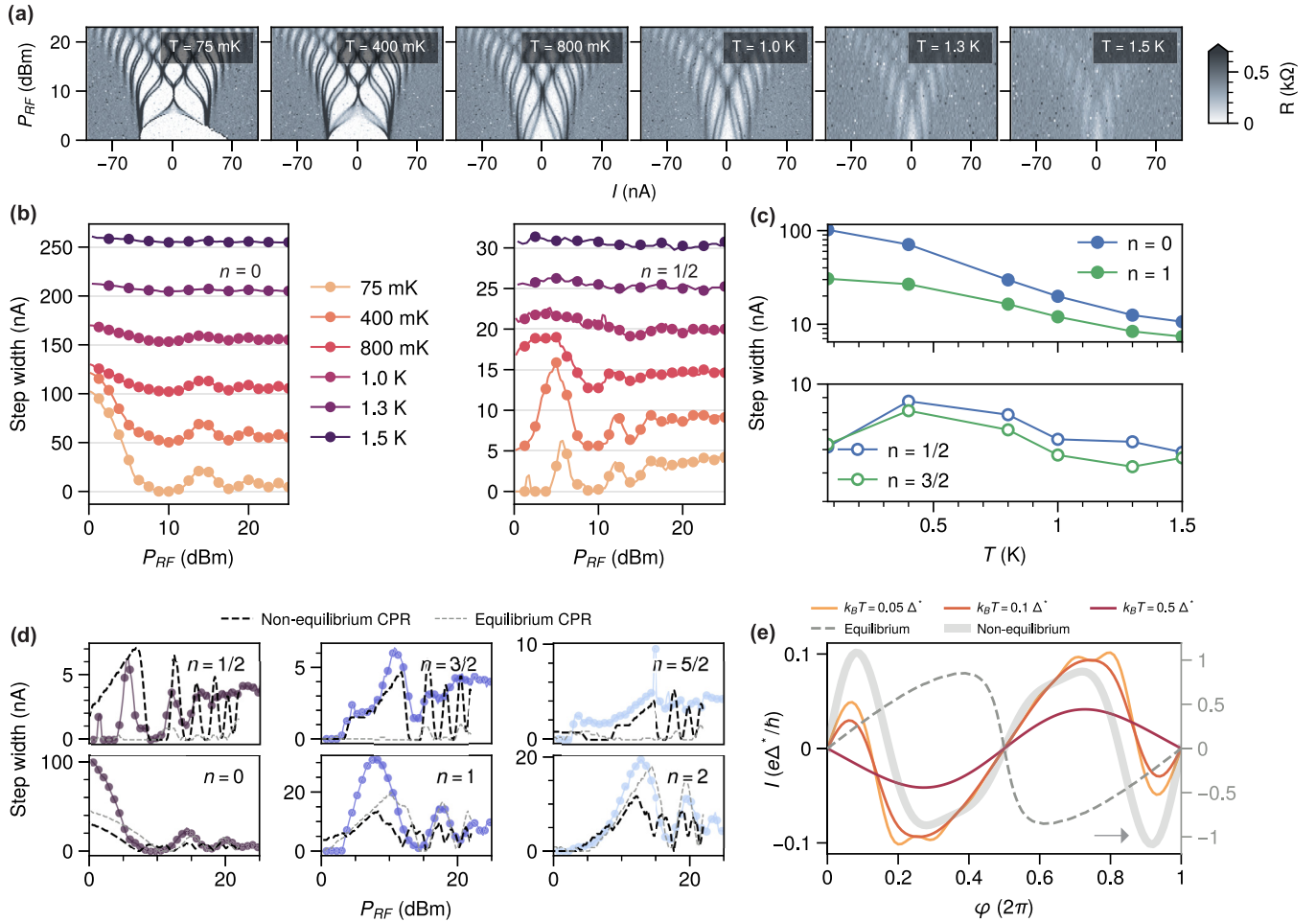


FIG. 3. (a) Shapiro maps at different temperatures $T = (75 \text{ mK}, 400 \text{ mK}, 800 \text{ mK}, 1.0 \text{ K}, 1.3 \text{ K}, 1.5 \text{ K})$ at $f = 1.75 \text{ GHz}$. (b) Step width for $n = 0$ (left) and $n = 1/2$ (right) extracted from the temperature maps show in (a). As temperature increases, a monotonic decrease is observed for $n = 0$, while a nonmonotonic evolution with a maximum at 400 mK is observed for $n = 1/2$. Traces are offset for clarity, with an offset of 50 nA (left) and 5 nA (right). (c) Step widths displayed on a semilog scale as a function of T for integers $n = 0, 1$ (top) and half-integers $n = 1/2, 3/2$ (bottom). Microwave powers $P_{RF} = 0 \text{ dBm}$ for $n = 0$, $P_{RF} = 8 \text{ dBm}$ for $n = 1$, $P_{RF} = 5.5 \text{ dBm}$ for $n = 1/2$, and $P_{RF} = 11 \text{ dBm}$ for $n = 3/2$. (d) Step width of half-integer $n = 1/2, 3/2, 5/2$ (top) and integer $n = 0, 1, 2$ (bottom). Each trace is a horizontal slice of Fig. 2(c). The dashed black lines represent the numerical simulations obtained from the extended RCSJ model using the nonequilibrium CPR shown as the thick gray line in (e). The dashed gray lines represent the simulations using the equilibrium CPR. (e) CPRs under microwave irradiation for $\tau = 0.98$ and driving $w = 1.3$ at different temperatures ($k_B T = 0.05, 0.1, \text{ and } 0.5 \Delta^*$) are depicted by light to dark orange lines. The dashed gray line represents the equilibrium CPR at $w = 0$ and $k_B T = 0.05 \Delta^*$, for the same value of τ . The thick gray line represents the effective nonequilibrium CPR used in (d).

circuit feedback [40,76,77] can also contribute to the appearance of fractional steps or hysteretic behavior. Subharmonic structures may also indicate a unique mode of a more complex circuit network, as seen in junction arrays [78–83] and superconducting quantum interference devices (SQUIDs) [80,84,85]. These manifestations are also visible even in the absence of multiple superconducting terminals, as in grain boundary or step-edge junctions [86–89], as a consequence of the complex evolution of multiple phase-locked states.

The fractional steps reported in the previous examples, including both ballistic and diffusive SNS junctions, are ascribed to the equilibrium properties of the supercurrent and can be understood within a phenomenological extended resistively and capacitively shunted junction (RCSJ) model, which takes into account the dissipative environment surrounding the junction, as depicted in Fig. 1(c) [3,40,41]. In

the phase-particle picture, neglecting capacitive effects, the phase evolves in a washboard potential that is tilted by the applied bias current and modulated by the time-dependent drive. Shapiro steps arise as time-dependent phase slips between the minima of the Josephson potential, and for a typical $\sin(\varphi)$ CPR, integer steps arise as $2\pi n$ phase slips. Within this picture, half-integer Shapiro steps require an energy-phase relation that displays a secondary minimum and arise when the second harmonic of the CPR is stronger than the first one.

However, a microwave drive can also significantly alter the supercurrent’s steady-state behavior, exciting nonequilibrium supercurrents [5,37,62–66,90–97]. The adiabatic changes in the ABS energies, as well as the multiple transitions induced by microwave photons between the ABSs or between the ABSs and the continuum, can result in a nontrivial dynamics

of the supercurrent-carrying states [62,93,95,96]. Such effects can give rise to highly distorted CPRs, which exhibit sign reversals of the supercurrent and π -periodic oscillations at twice the Josephson frequency [5,63,64,90,92,94,98].

We notice that in the experiment the induced gap $\Delta^* \simeq 280 \mu\text{eV}$ (67 GHz), so that we cover values $hf \simeq 0.03 \Delta^*$. In an effort to capture the emergence of half-integer Shapiro steps, we describe the junction dynamics by adiabatically incorporating nonequilibrium effects into the RCSJ model of Fig. 1(c) through a single effective CPR. The latter is provided by the thick gray line in Fig. 3(e), and its origin will be discussed later. In Fig. 3(d) we plot the step width for integer and half-integer values of n vs P_{RF} , obtained as horizontal slices of Fig. 2(c) at constant V . The dashed black line in the figure shows the results of the simulation using the effective nonequilibrium CPR, while the dashed gray line represents the equilibrium one. Although the equilibrium CPR effectively reproduces the integer steps in the oscillatory pattern (bottom row), it completely fails to capture the half-integer steps (top row). This is despite the presence of higher-order harmonics in the highly skewed CPR, which are often attributed to the origin of half-integer steps [67].

To gain further insight into the origin of such a distorted CPR, we used a tight-binding method within the Keldysh-Green's function approach [93,96] to numerically calculate the current-phase relationship of an SNS junction irradiated by a microwave tone. The model describes a single-channel Josephson junction with an arbitrary junction transparency τ and gap Δ^* . The microwave driving is included as a time-dependent modulation of the phase difference across the junction with amplitude $w = eV_{\text{RF}}/hf$. Figure 3(e) shows the simulated CPR for microwave irradiation of $hf = 0.1 \Delta^*$ at a microwave driving of $w \sim 1.3$ and $\tau = 0.98$ for different temperatures. The dashed gray line represents the equilibrium CPR. The microwave irradiation significantly alters the CPR, boosting a strong second harmonic, which results in the development of an additional minimum. This provides insight into the origin of the effective nonequilibrium CPR used in the RCSJ model. The wiggles in the CPR are due to nonequilibrium population of Floquet sidebands produced by the microwave driving and disappear at temperatures on the order of the driving frequency, $k_B T \sim hf$. In turn, the secondary minimum is robust and still visible at $k_B T = 0.1 \Delta^*$, as shown in Fig. 3(e), and it qualitatively agrees with the robustness of the half-integer steps with respect to temperature. In Appendix H we detail the theoretical model and present additional simulations showing that reducing the junction transparency results in the disappearance of the CPR's secondary minimum (Fig. 13).

The outlined procedure should be regarded as an attempt to reconcile the results of the adiabatic approximation, typical of the RCSJ model, with the microscopically calculated CPR in the presence of microwave driving and in the absence of a steady voltage across the junction. In particular, the model reproduces the two-minima shape of the effective nonequilibrium CPR only within a limited range of w values, which is inconsistent with the experimental observations and highlights the limitations of the present description. Alternative phenomenological theories of nonequilibrium supercurrents have been proposed [5,63,90] which model the system by

considering both the ABSs and their occupation distributions oscillating at the Josephson frequency. The specific structure of the ABSs, including the effects of finite junction length or ballistic quasi-two-dimensional transport, may be responsible for the discrepancies between different predictions, which calls for more comprehensive theories.

In conclusion, we have investigated a highly transmissive Josephson junction made of an InSb nanoflag with Nb contacts. Our results indicate strong evidence of parallel transport in both long and short conducting channels, confirmed by the temperature-dependent supercurrent and magnetic field interference. Under microwave irradiation, we observe strong half-integer Shapiro steps, showing a nonmonotonic temperature evolution that points to nonequilibrium effects induced by the driving. The observed phenomenology is only partially captured by the predictions based on the adiabatic approximation in terms of a nonequilibrium CPR. Further theoretical developments are needed to address the presence of strong second harmonic supercurrents in ballistic, highly transparent SNS junctions. Future experiments should investigate the potential of InSb nanoflag Josephson junctions for exploring the coherent manipulation of Andreev states and their nonequilibrium dynamics.

ACKNOWLEDGMENTS

The authors thank Daniele Ercolani for his help with the growth of the InSb nanoflags and Michal Nowak, Gorm Ole Steffensen, and Alfredo Levy Yeyati for useful discussions. This research activity was partially supported by the FET-OPEN project AndQC (H2020 Grant No. 828948), PNRR MUR Project No. PE0000023-NQSTI, and PRIN MUR (Grant No. 2022PH852L). E.S. and F.G. acknowledge the EU's Horizon 2020 research and innovation program under Grant Agreements No. 800923 (SUPERTEC) and No. 964398 (SUPERGATE) for partial financial support.

APPENDIX A: SAMPLE INFORMATION AND MEASUREMENT TECHNIQUES

The InSb nanoflags utilized in this work have been extensively described in previous studies [23,28]. They are defect-free structures that exhibit excellent electrical properties, including high mobility (up to $29\,500 \text{ cm}^2 \text{ V}^{-1} \text{ s}^{-1}$) and a large mean free path ($l_e \simeq 500 \text{ nm}$) at $T = 4.2 \text{ K}$. The devices were fabricated by placing nanoflags on a p -doped Si/SiO₂ substrate, which served as a backgate, and connecting them with 150 nm of Nb deposited via DC magnetron sputtering at a deposition rate of approximately 1 nm s^{-1} in a chamber with a base pressure of $2 \times 10^{-6} \text{ mbar}$. Prior to metal deposition, a passivation step was performed to improve the semiconductor-metal transparency. The critical temperature of Nb was measured to be 8.9 K on two independently connected electrodes on the same device, corresponding to a gap $\Delta = 1.76 k_B T_c \sim 1.35 \text{ meV}$. Further information on device fabrication can be found in the supporting material of Refs. [30,31]. We conducted transport measurements using a low-temperature Leiden Cryogenics dilution refrigerator with a base temperature of 75 mK. The cryostat is equipped with a three-level filtering system, comprising π filters at room

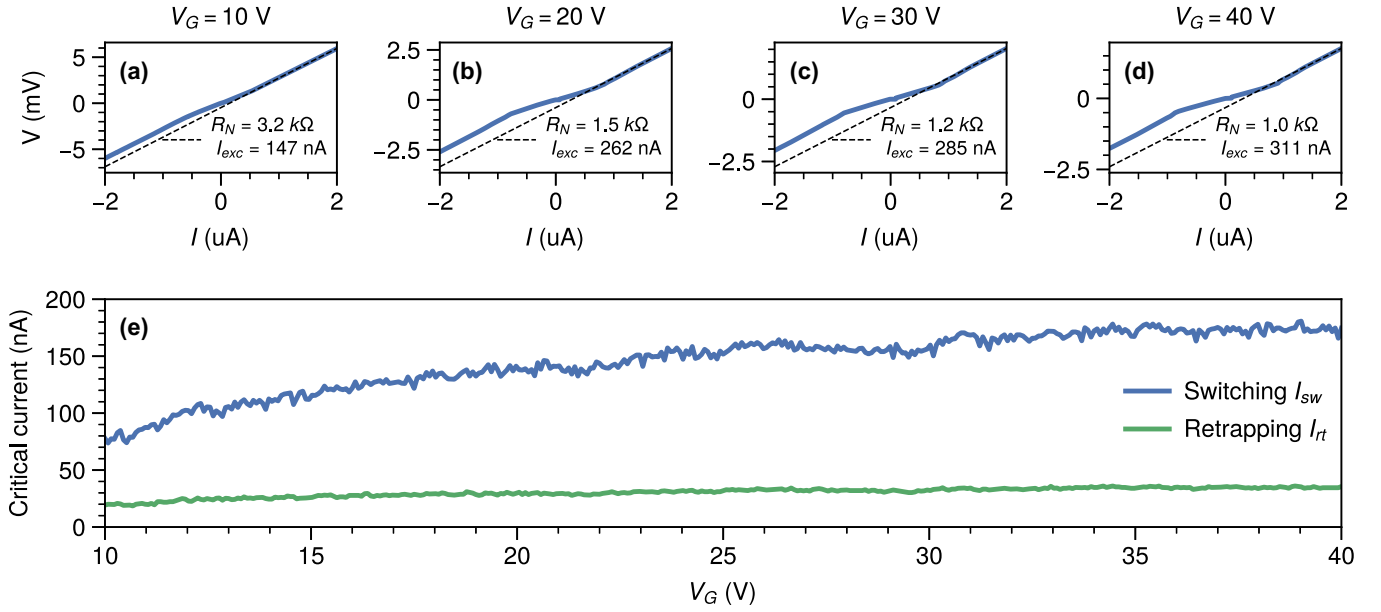


FIG. 4. (a)–(d) Sample I - V traces for different V_G values (10, 20, 30, 40) V. The black dashed line is the linear fit to the Ohmic region used to extract R_N and I_{exc} . (e) Full backgate dependence of the switching and retrapping current in the same gate voltage range.

temperature as well as cryogenic π and RC filters at base temperature. The $V(I)$ curves were acquired in a standard four-wire configuration, with the junction current-biased using a Yokogawa GS200 voltage source over a 10 M Ω resistor. The voltage drop over the junction was amplified by a factor 1000 using a room temperature DL1201 voltage preamplifier operated in battery mode and acquired by an Agilent 34410 multimeter. We applied voltage to the backgate using a Keithley 2602 voltage source. Microwave signals were applied using an R&S SMR20 microwave source to an attenuated semirigid open-ended coaxial cable in close proximity to the sample holder, which had been attenuated by 20 dB and 10 dB at 3K and Cold plates, respectively. For measurements in magnetic field, we used a low-noise Keithley 2400 sourceme-ter connected to a 2 T American Magnetics magnet.

APPENDIX B: DEPENDENCE ON BACKGATE VOLTAGE

Figures 4(a)–(d) display $V(I)$ curves in a higher current range at different backgate voltages V_G ranging from 10 V to 40 V. For negative gate voltages, the InSb nanoflag is insulating, and no supercurrent can flow. The black dashed line fitted to the Ohmic region allows obtaining the normal state resistance R_N and excess current I_{exc} . In Fig. 4(e) we present the switching current I_{sw} and retrapping current I_{rt} over the

same range of gate voltages. The switching current I_{sw} decreases from 170 nA to 75 nA as the gate voltage is varied, while the retrapping current I_{rt} remains roughly constant at approximately 30 nA.

Figure 5(a) depicts the evolution of R_N and $G_N = 1/R_N$ as a function of V_G , with the resistance decreasing from 3 k Ω (at $V_G = 10$ V) to 1 k Ω (at $V_G = 40$ V). The high transparency of the junction is confirmed by the high values of the excess current I_{exc} and the $I_{sw}R_N$ product. Figure 5(b) shows the excess current as a function of V_G in the same range. The product $I_{exc}R_N$ remains roughly constant at about 350 μV ($1.2 \Delta^*/e$) over the entire gate voltage range, close to the theoretical value of $8/3 \Delta^*/e$ predicted for the ballistic case [Fig. 5(c)] [99]. Moreover, the product $I_{sw}R_N$ is expected to be $I_{sw}R_N = 10.82 E_{Th}/e$ for a long diffusive junction in the limit $\Delta^* \gg E_{Th}$ [48]. In our device, $I_{sw}R_N$ varies from 180 μV to 250 μV ($7 - 10 E_{Th}/e$) [Fig. 5(d)]. Additionally, we can estimate the transparency of the superconductor-semiconductor interface to be $\gamma_B \sim 7$ [100], which is almost half the value reported in [30], confirming the increased transparency.

APPENDIX C: MAGNETIC INTERFERENCE MAPS

Figures 6 and 7 present additional measurements of magnetic interference patterns at different temperatures,

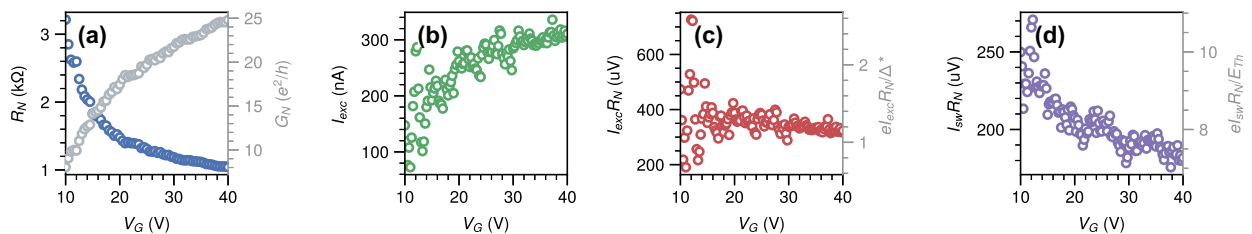


FIG. 5. (a) Normal state resistance R_N , (b) excess current I_{exc} , (c) $I_{exc}R_N$ product, and (d) $I_{sw}R_N$ product plotted as functions of the backgate voltage V_G .

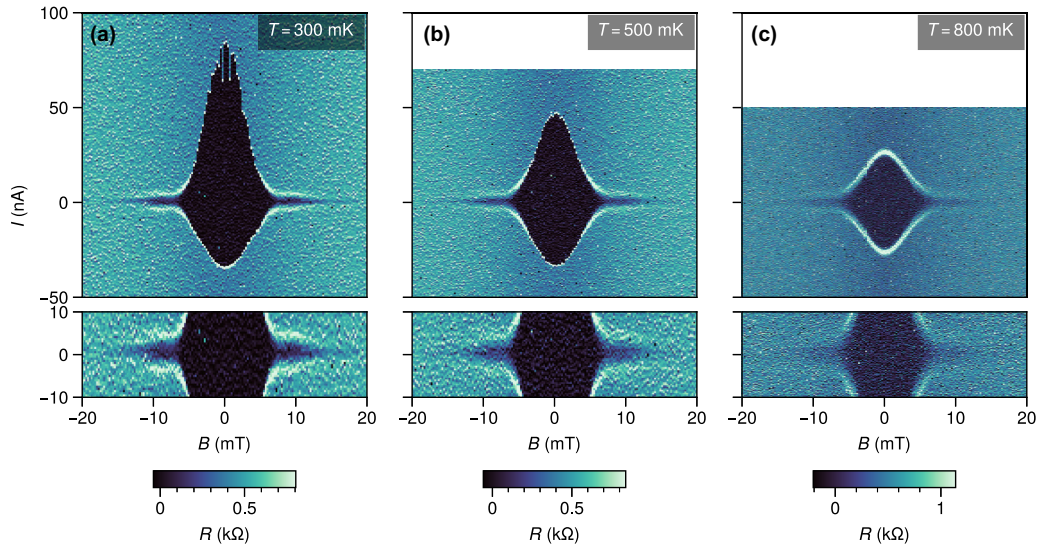


FIG. 6. Magnetoresistance maps at temperatures of (a) 300 mK, (b) 500 mK, and (c) 800 mK. Below each panel, a zoom-in on the low-bias region shows the behavior of the side lobes with respect to T .

$T = (300, 500, 800)$ mK, and backgate voltages, $V_G = (30, 20, 10)$ V. The magnetoresistance maps in Fig. 6 demonstrate a decrease in the Gaussian-like contribution as the temperature increases, further confirming that the exponential suppression of I_{sw} is related to states in the long junction limit. The Fraunhofer diffraction side lobes remain unchanged up to a temperature of 500 mK, consistent with the limited dependence of $I_{sw}(T)$ for modes in the short junction limit, and eventually begin to disappear only for $T > 800$ mK.

Figure 7 shows the magnetoresistance evolution in V_G . States in the long junction limit are more sensitive to changes in the semiconductor depletion level at low gate voltages V_G , as evidenced by the corresponding changes in the Gaussian

amplitude. Only a little variation of the Fraunhofer diffraction lobes is observed, confirming the high homogeneity of the current density in the short junction area between the electrodes.

APPENDIX D: SHAPIRO MAPS AT FINITE MAGNETIC FIELD

Figure 8 depicts the Shapiro maps obtained at a frequency of $f = 1.75$ GHz for different out-of-plane magnetic field values ranging from 0 to 11 mT. As the magnetic field suppresses I_c , the reduced drive frequency $\Omega = \frac{2\pi f}{2el_c R_j/\hbar}$ increases, and the $V(I)$ maps follow the Bessel function dependence on the applied RF power [40,41].

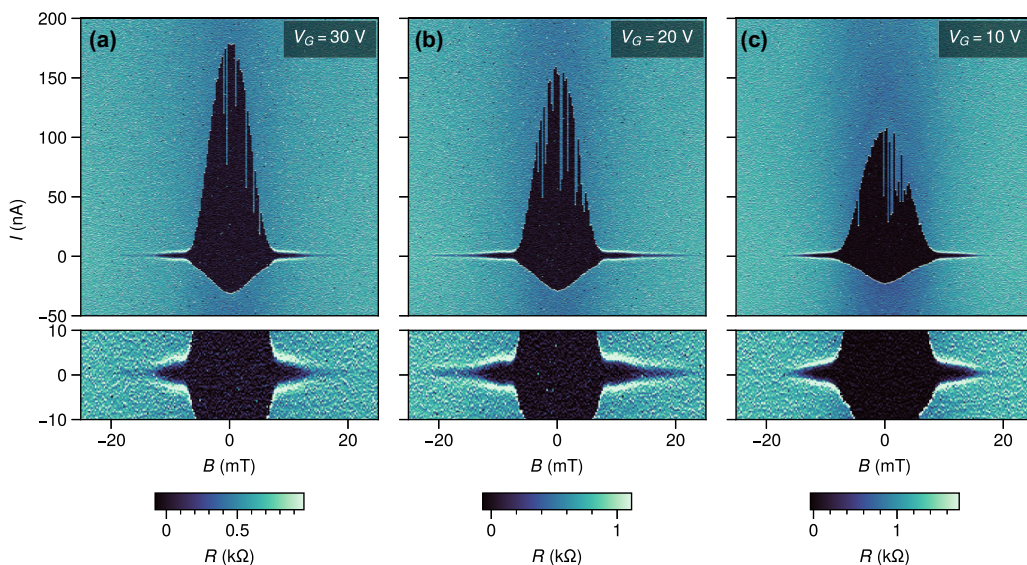


FIG. 7. Magnetoresistance maps at backgate voltage V_G of (a) 30 V, (b) 20 V, and (c) 10 V. Below each panel, a zoom-in on the low-bias region shows the behavior of the side lobes with respect to V_G .

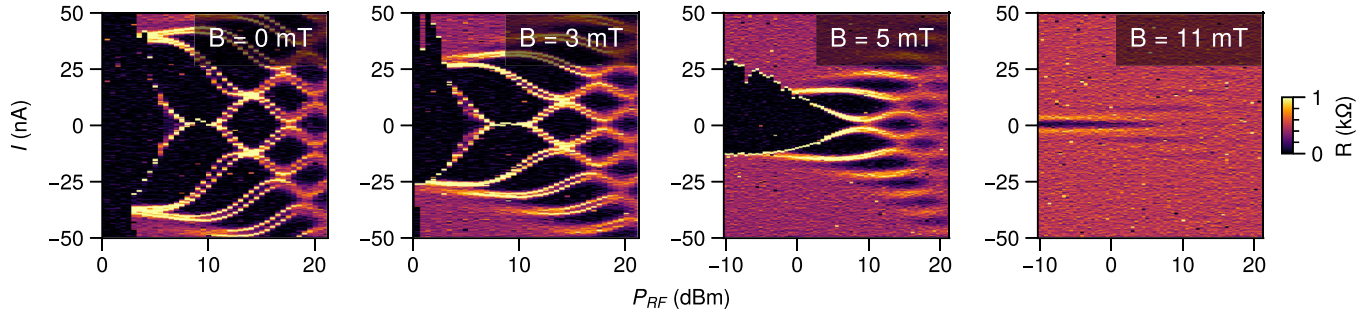


FIG. 8. Shapiro maps at $f = 1.75$ GHz for various out-of-plane magnetic field strengths B ranging from 0 to 11 mT.

APPENDIX E: SHAPIRO MAPS AT DIFFERENT BACKGATE VOLTAGES AND TEMPERATURES

The evolution of the half-integer steps is robust in temperature and backgate voltage, as detailed by the scans in Fig. 9 for $V_G = 40$ V (top row) and $V_G = 10$ V (bottom row).

± 1 lobes. The presence of zero-crossing steps has been extensively investigated in Larson *et al.* [41] and explained as a consequence of the shunting RC environment and the high $I_c R_j$ product.

APPENDIX F: SHAPIRO MAPS AT ZERO CROSSING STEP

We present in Fig. 10 a more detailed scan of the Shapiro map at $f = 1.75$ GHz, covering a restricted range of microwave power and currents as shown in Fig. 2. Zero-crossing steps (red line) are visible as a result of the overlapping

APPENDIX G: DATA FROM AN ADDITIONAL DEVICE WITH LOWER TRANSPARENCY

An additional device has been measured in a similar way, which had a 5 nm Ti adhesion layer embedded under the niobium layer. In this case, only weak signatures of half-integer steps are visible, as can be seen in Fig. 11.

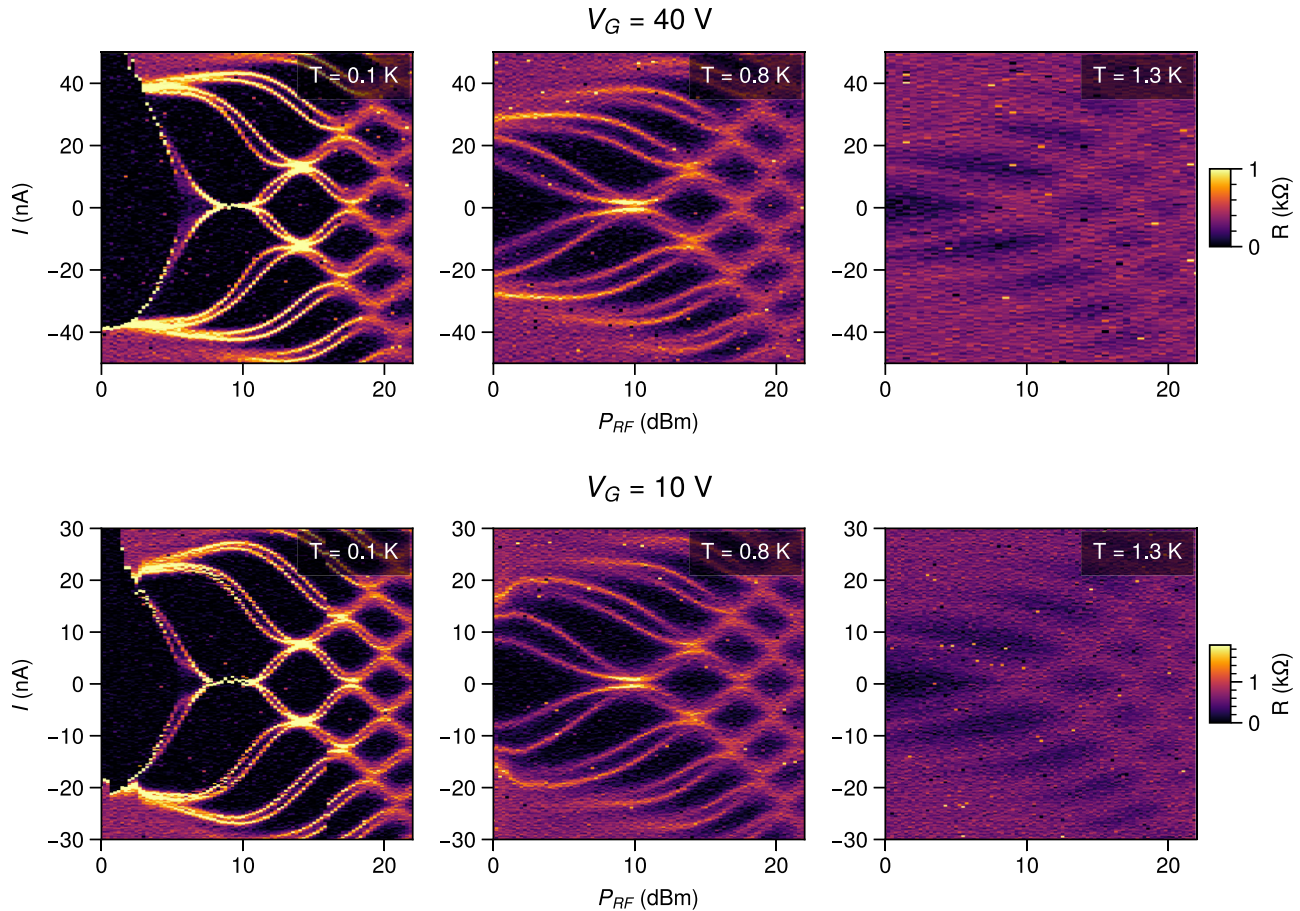


FIG. 9. Top row: Shapiro maps at $f = 1.75$ GHz for different temperatures of 0.1 K, 0.8 K, and 1.3 K at a backgate voltage of 40 V. Bottom row: same maps for a backgate voltage of 10 V.

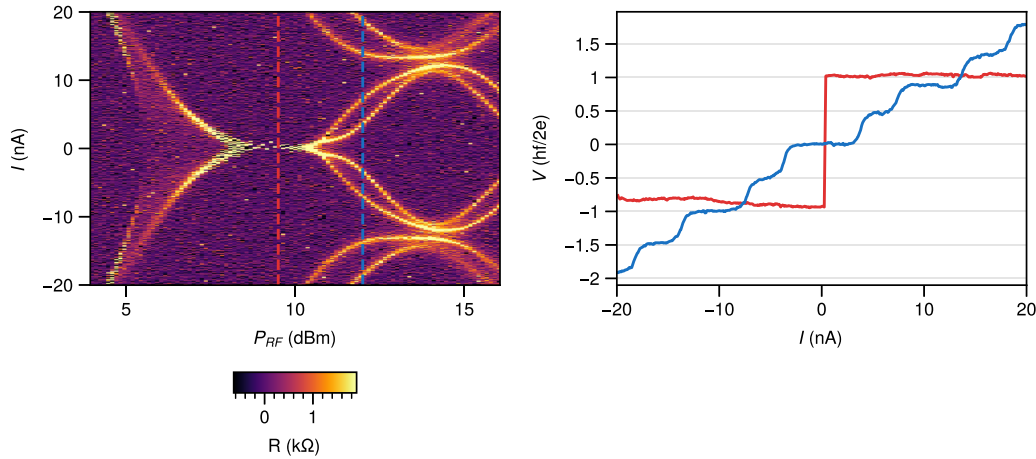


FIG. 10. Left: A zoom-in view of the Shapiro maps at $f = 1.75$ GHz, as shown in Fig. 2, highlighting the zero-crossing steps and providing finer details of the half-integer plateaus. Right: The red and blue $V(I)$ cut shown on the left for $P_{RF} = 9$ dBm and $P_{RF} = 12$ dBm, respectively.

APPENDIX H: THEORY

1. CPR under microwave irradiation

Our microscopic model for a microwave-irradiated Josephson junction is based on Refs. [93,96,101] and consists of a highly transparent junction, with a short ballistic region between the left and right superconducting leads (L and R, respectively), as schematically displayed in Fig. 12(a). We describe the system through the 1D tight-binding Hamiltonian $H = H_L + H_R + \sum_{\sigma} (v c_{L\sigma}^{\dagger} c_{R\sigma} + v^* c_{R\sigma}^{\dagger} c_{L\sigma})$, where the left and right leads are described by $H_{\alpha} = -\mu \sum_{n\sigma} c_{\alpha,n,\sigma}^{\dagger} c_{\alpha,n,\sigma} - t \sum_{n,\sigma} (c_{\alpha,\sigma,n}^{\dagger} c_{\alpha,\sigma,n+1} + \text{H.c.}) + \Delta_{\alpha} \sum_n c_{\alpha,n,\uparrow}^{\dagger} c_{\alpha,n,\downarrow} + \text{H.c.}$, with c and c^{\dagger} being the annihilation and creation operators for particles with spin σ in the superconducting leads and $\Delta_{\alpha} = \Delta e^{i\varphi_{\alpha}}$, with $\varphi_R - \varphi_L = \varphi$ their phase difference. The normal state transmission of this single channel model is $\tau = \frac{4(v/W)^2}{(1+(v/W)^2)^2}$, where $W = 1/(\pi\rho_F) = \sqrt{4t^2 - \mu^2}/2$ and ρ_F is the density of states at the Fermi energy in the leads. The current takes the form $\hat{I}(t) = \frac{ie}{\hbar} \sum_{\sigma} (v c_{L\sigma}^{\dagger} c_{R\sigma} - v^* c_{R\sigma}^{\dagger} c_{L\sigma})$, and under microwave irradiation, the phase difference acquires the time dependence $\varphi(t) = \varphi_0 + 2w \sin(2\pi ft)$ with $w = eV_{ac}/hf$, so that $v \rightarrow v e^{i\varphi(t)/2}$.

The microwave source can inject and absorb photons of frequency f , so that an incident carrier with energy ϵ can be scattered into states with energy $\epsilon + nhf$.

Introducing the Floquet sidebands, which are replicas of the system shifted in energy by nhf , the hopping term \hat{v}_{LR} can couple different sidebands $\hat{v}_{n,m} = \int dt e^{i(n-m)2\pi ft} \hat{v}(t) = v \begin{pmatrix} J_{n-m}(w)e^{i\varphi_0/2} & 0 \\ 0 & -J_{m-n}(w)e^{-i\varphi_0/2} \end{pmatrix}$, where $J_n(w)$ are Bessel functions of the first kind, and we have absorbed the possible phase of v in the phase difference φ_0 . The hopping between the L and R leads acquires a matrix structure that connects the rightmost site in the L lead and Floquet band n with the leftmost site of the R lead and Floquet band m , as schematized in Fig. 12(b).

We now apply the microscopic theory and calculate different CPRs under microwave irradiation. In the absence of driving ($w = 0$), the model accurately reproduced the CPRs of the junction in both the highly transparent and tunneling regimes by varying the ratio v/t , as shown in Fig. 13(a), and for different temperatures, as shown in Fig. 13(b). We then apply increasing microwave driving and observe a second zero of the CPR in the interval $0-\pi$, along with a region of negative current for positive phase bias, which indicated the occurrence of a secondary minimum [Fig. 13(c)]. At high driving amplitude, the CPR exhibits wiggles due to the presence of Floquet sidebands, which decay with temperature, as shown in Fig. 3(e). Finally, Fig. 13(d) shows that the CPR loses its secondary zero for low transmission. These features are qualitatively similar to those observed in the additional device

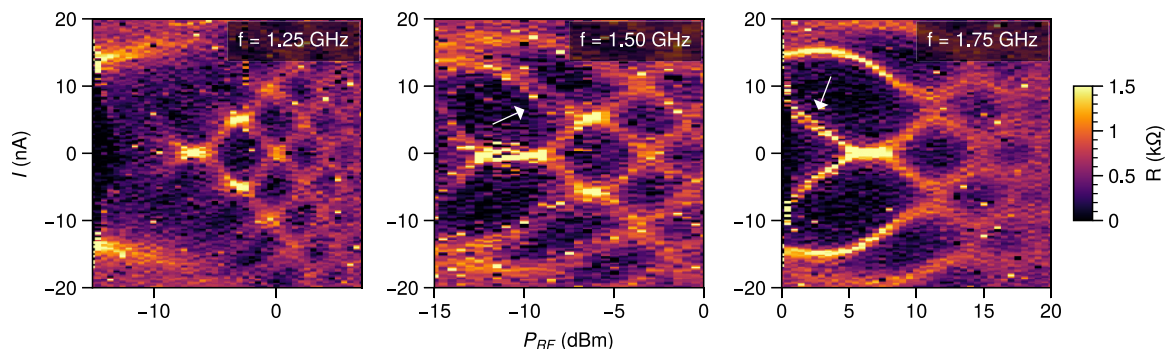


FIG. 11. Shapiro maps for $f = 1.25, 1.50,$ and 1.75 GHz for a device with reduced transparency.

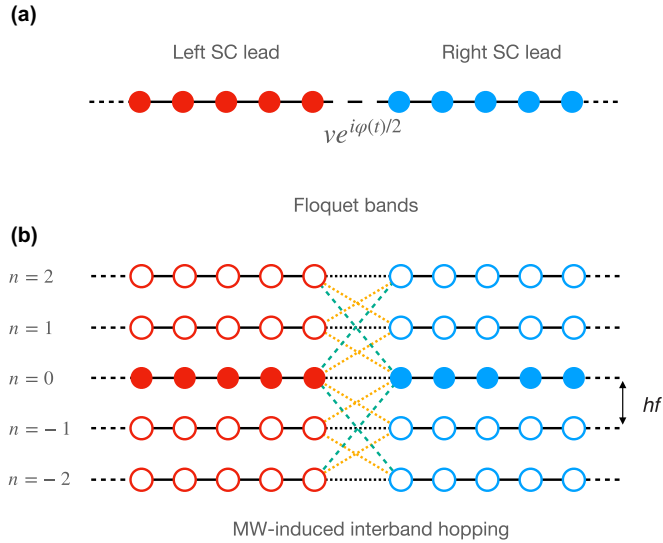


FIG. 12. (a) 1D tight-binding model describing the Josephson junction. The driving appears as a time-dependent phase in the left-right hopping amplitude. (b) Floquet side bands shifted in energy by nhf . The different bands are coupled at the interface by the time-oscillating phase.

reported in the experiment. Including additional bands up to six does not qualitatively change the discussion above.

2. RCSJ model

In the previous section, we described the microscopic theory of nonequilibrium supercurrents in a microwave-irradiated Josephson junction in the presence of an AC voltage bias. However, modeling the time-dependent phase dynamics in the presence of nonequilibrium effects, particularly for the experimentally relevant current-bias scenario, is more challenging. Moreover, we find that the environment surrounding the junction plays an important role, as confirmed by the deviations from the Bessel regime and the presence of zero-crossing steps. We opted for a simplistic approach that employs a modified version of the resistively and capacitively shunted junction (RCSJ) model, which includes the

dissipative environment surrounding the junction [3,41] and incorporates the nonequilibrium effects only in a single effective CPR. Despite the simplicity of the assumptions, we are able to capture the main findings of this work. The junction, which has a critical current I_c , is shunted by a capacitance C_j and resistance R_j , and is additionally shunted by an RC environment represented by a parallel capacitor C and resistor R . The entire circuit is biased by a current I , which accounts for the external DC and AC bias. The equations for the current I and the voltage V , shown in Fig. 1(c), are

$$\begin{aligned} I &= I_{\text{DC}} + I_{\text{RF}} \sin(2\pi ft) \\ &= C \frac{dV}{dt} + \text{CPR}(\varphi) + \frac{\hbar}{2eR_j} \frac{d\varphi}{dt} + \frac{\hbar C_j}{2e} \frac{d^2\varphi}{dt^2} \\ V &= \frac{\hbar}{2e} \frac{d\varphi}{dt} + R \left(\text{CPR}(\varphi) + \frac{\hbar}{2eR_j} \frac{d\varphi}{dt} + \frac{\hbar C_j}{2e} \frac{d^2\varphi}{dt^2} \right), \quad (\text{H1}) \end{aligned}$$

where φ is the macroscopic phase difference across the junction, I_{DC} and I_{RF} are the DC and RF current biases, respectively, and $\text{CPR}(\varphi)$ is the junction's current-phase relationship. We use a fourth-order Runge-Kutta method to solve for $\varphi(t)$ and obtain the DC voltage across the junction as $V_j = \langle \frac{\hbar}{2e} \frac{d\varphi}{dt} \rangle$.

In the limit of small I_c , the Shapiro map follows the Bessel function dependence, with steps centered at $I_n = \frac{V_n}{R_j}$ and an extension of $\sim I_c |J_n(2w)|$, where $V_n = n \frac{\hbar f}{2e}$ and $w = eV_{\text{AC}}/hf$. Figure 14(a) shows the Shapiro map at lower I_c with an applied external magnetic field of $B = 5$ mT. From the position of the centers, we can extract $R_j \sim 420 \Omega$ (dotted white lines), while the continuous lines show a good agreement with the Bessel behavior, depicting the amplitudes $I_c |J_n(2w)|$, with $V_{\text{AC}} = \alpha \times 10^{P_{\text{RF}}/20}$, $\alpha \sim 0.8$ and $I_c \sim 10$ nA.

Figures 14(b) and 14(c) show the complete maps for the simulation presented in Fig. 3(d) for the equilibrium and nonequilibrium CPRs, respectively, obtained by the model in Eq. (H1). While the equilibrium CPR well describes the overall trend, it completely lacks half-integer steps, which are instead captured by the effective nonequilibrium CPR. This is despite the presence of higher-order harmonics in the skewed equilibrium CPR. In the simulation, we estimate the geometric

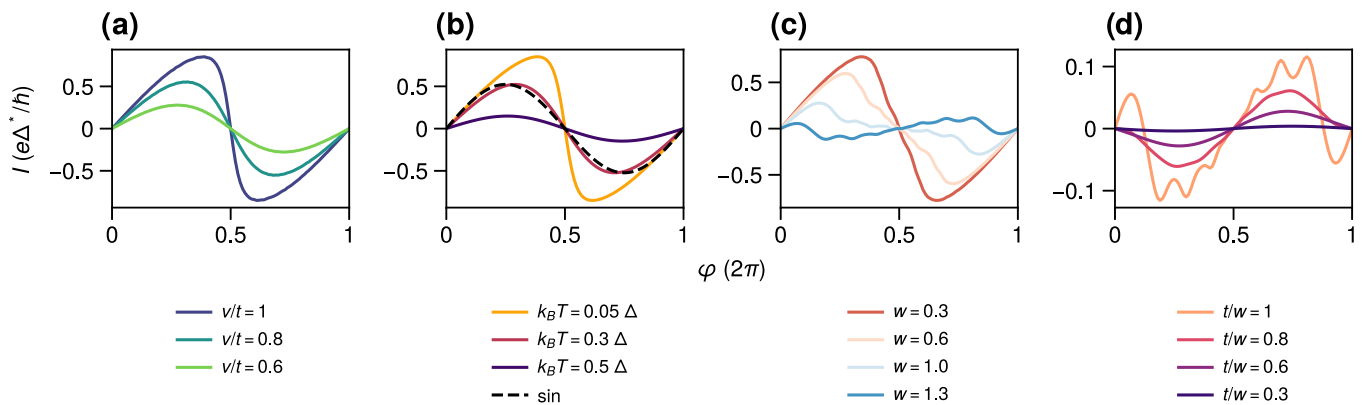


FIG. 13. Different CPRs: (a) in the absence of microwave irradiation for different transparencies, (b) in the absence of microwave irradiation for different temperatures, (c) for different microwave drive strengths at $v/t = 1$, and (d) for different transparencies at driving $w = 1.3$.

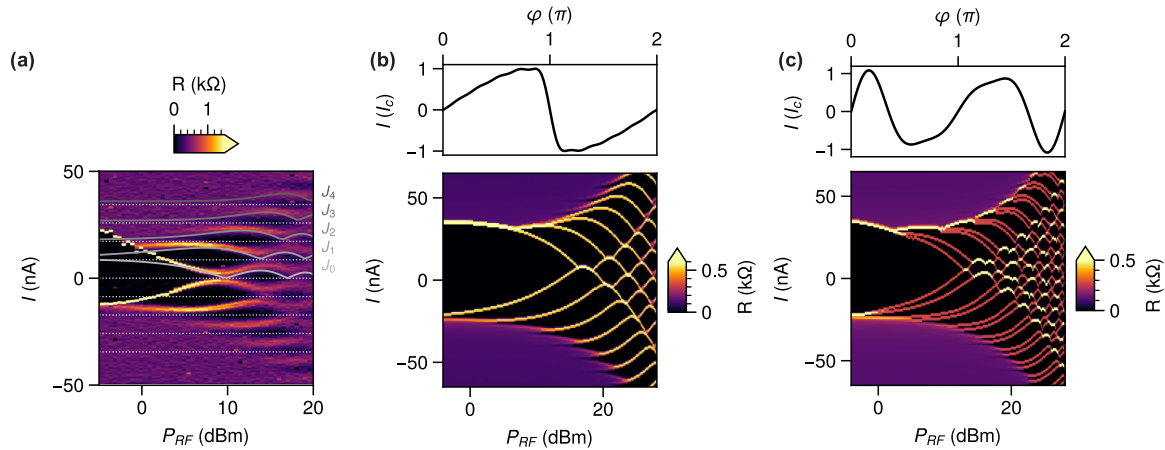


FIG. 14. (a) Experimentally measured Shapiro map in the Bessel regime at $B = 5$ mT. The dotted white lines are used to extract R_j , while the continuous lines show the dependence on the Bessel function J_n . (b) Numerical simulation of the Shapiro map with the equilibrium skewed CPR. The amplitudes of the harmonics are $I_{c,n} = (0.91, -0.33, 0.19, -0.12, 0.09, -0.06, 0.04, -0.03, 0.03, -0.02)$. (c) Same as in (b) for the effective nonequilibrium CPR with the amplitudes $I_{c,n} = (-0.38, 0.75, 0.44, 0.22)$.

capacitance of the junction to be \sim fF and neglect C_j . The capacitance C is determined by the bonding pads' capacitance to the SiO_2 backgate, which we estimate to be $C \sim 15$ pF, while the value of R is set to $R \sim 150 \Omega$ to achieve the best

agreement with the experiment. The CPR is expressed as $\text{CPR}(\varphi) = \sum_n I_{c,n} \sin(n\varphi)$, where $I_c = \max_\varphi \text{CPR}(\varphi)$, which is set to 35 nA. The current I_{RF} is given by $I_{\text{RF}} = \beta \times 10^{P_{\text{RF}}/20}$ with $\beta \sim 20$.

- [1] I. O. Kulik, Macroscopic quantization and the proximity effect in S-N-S junctions, *Sov. Phys. JETP* **30**, 944 (1970).
- [2] B. Pannetier and H. Courtois, Andreev reflection and proximity effect, *J. Low Temp. Phys.* **118**, 599 (2000).
- [3] P. Jarillo-Herrero, J. A. van Dam, and L. P. Kouwenhoven, Quantum supercurrent transistors in carbon nanotubes, *Nature (London)* **439**, 953 (2006).
- [4] V. E. Calado, S. Goswami, G. Nanda, M. Diez, A. R. Akhmerov, K. Watanabe, T. Taniguchi, T. M. Klapwijk, and L. M. K. Vandersypen, Ballistic Josephson junctions in edge-contacted graphene, *Nat. Nanotechnol.* **10**, 761 (2015).
- [5] K. W. Lehnert, N. Argaman, H.-R. Blank, K. C. Wong, S. J. Allen, E. L. Hu, and H. Kroemer, Nonequilibrium ac Josephson Effect in Mesoscopic Nb-InAs-Nb Junctions, *Phys. Rev. Lett.* **82**, 1265 (1999).
- [6] F. Giazotto, K. Grove-Rasmussen, R. Fazio, F. Beltram, E. H. Linfield, and D. A. Ritchie, Josephson current in Nb/InAs/Nb highly transmissive ballistic junctions, *J. Supercond.* **17**, 317 (2004).
- [7] C. T. Ke, C. M. Moehle, F. K. de Vries, C. Thomas, S. Metti, C. R. Guinn, R. Kallaher, M. Lodari, G. Scappucci, T. Wang *et al.*, Ballistic superconductivity and tunable π -junctions in InSb quantum wells, *Nat. Commun.* **10**, 3764 (2019).
- [8] H. Sellier, C. Baraduc, F. Lefloch, and R. Calemczuk, Half-Integer Shapiro Steps at the $0-\pi$ Crossover of a Ferromagnetic Josephson Junction, *Phys. Rev. Lett.* **92**, 257005 (2004).
- [9] S. M. Frolov, D. J. Van Harlingen, V. V. Bolginov, V. A. Oboznov, and V. V. Ryazanov, Josephson interferometry and Shapiro step measurements of superconductor-ferromagnet-superconductor $0-\pi$ junctions, *Phys. Rev. B* **74**, 020503(R) (2006).
- [10] M. Veldhorst, M. Snelder, M. Hoek, T. Gang, V. K. Guduru, X. L. Wang, U. Zeitler, W. G. van der Wiel, A. A. Golubov, H. Hilgenkamp, and A. Brinkman, Josephson supercurrent through a topological insulator surface state, *Nat. Mater.* **11**, 417 (2012).
- [11] S. Hart, H. Ren, T. Wagner, P. Leubner, M. Mühlbauer, C. Brüne, H. Buhmann, L. W. Molenkamp, and A. Yacoby, Induced superconductivity in the quantum spin Hall edge, *Nat. Phys.* **10**, 638 (2014).
- [12] V. S. Pribiag, A. J. A. Beukman, F. Qu, M. C. Cassidy, C. Charpentier, W. Wegscheider, and L. P. Kouwenhoven, Edge-mode superconductivity in a two dimensional topological insulator, *Nat. Nanotechnol.* **10**, 593 (2015).
- [13] F. Qu, J. van Veen, F. K. de Vries, A. J. A. Beukman, M. Wimmer, W. Yi, A. A. Kiselev, B.-M. Nguyen, M. Sokolich, M. J. Manfra *et al.*, Quantized conductance and large g -factor anisotropy in InSb quantum point contacts, *Nano Lett.* **16**, 7509 (2016).
- [14] W. Mayer, W. F. Schiela, J. Yuan, M. Hatefipour, W. L. Sarney, S. P. Svensson, A. C. Leff, T. Campos, K. S. Wickramasinghe, M. C. Dartiailh *et al.*, Superconducting proximity effect in InAsSb surface quantum wells with in situ Al contacts, *ACS Appl. Electron. Mater.* **2**, 2351 (2020).
- [15] C. M. Moehle, C. T. Ke, Q. Wang, C. Thomas, D. Xiao, S. Karwal, M. Lodari, V. van de Kerkhof, R. Termaat, G. C. Gardner *et al.*, InSbAs two-dimensional electron gases as a platform for topological superconductivity, *Nano Lett.* **21**, 9990 (2021).

- [16] Z. Lei, C. A. Lehner, E. Cheah, C. Mittag, M. Karalic, W. Wegscheider, K. Ensslin, and T. Ihn, Gate-defined quantum point contact in an InSb two-dimensional electron gas, *Phys. Rev. Res.* **3**, 023042 (2021).
- [17] Y. Chen, S. Huang, J. Mu, D. Pan, J. Zhao, and H.-Q. Xu, A double quantum dot defined by top gates in a single crystalline InSb nanosheet, *Chin. Phys. B* **30**, 128501 (2021).
- [18] M. de la Mata, R. Leturcq, S. R. Plissard, C. Rolland, C. Magén, J. Arbiol, and P. Caroff, Twin-induced InSb nanosails: A convenient high mobility quantum system, *Nano Lett.* **16**, 825 (2016).
- [19] F. K. de Vries, M. L. Sol, S. Gazibegovic, R. L. M. op het Veld, S. C. Balk, D. Car, E. P. A. M. Bakkers, L. P. Kouwenhoven, and J. Shen, Crossed Andreev reflection in InSb flake Josephson junctions, *Phys. Rev. Res.* **1**, 032031(R) (2019).
- [20] D. Pan, D. X. Fan, N. Kang, J. H. Zhi, X. Z. Yu, H. Q. Xu, and J. H. Zhao, Free-standing two-dimensional single-crystalline InSb nanosheets, *Nano Lett.* **16**, 834 (2016).
- [21] J. Zhi, N. Kang, S. Li, D. Fan, F. Su, D. Pan, S. Zhao, J. Zhao, and H. Xu, Supercurrent and multiple Andreev reflections in InSb nanosheet SNS junctions, *Physica Status Solidi B* **256**, 1800538 (2019).
- [22] J. Zhi, N. Kang, F. Su, D. Fan, S. Li, D. Pan, S. P. Zhao, J. Zhao, and H. Q. Xu, Coexistence of induced superconductivity and quantum Hall states in InSb nanosheets, *Phys. Rev. B* **99**, 245302 (2019).
- [23] I. Verma, V. Zannier, F. Rossi, D. Ercolani, F. Beltram, and L. Sorba, Morphology control of single-crystal InSb nanostructures by tuning the growth parameters, *Nanotechnology* **31**, 384002 (2020).
- [24] N. Kang, D. Fan, J. Zhi, D. Pan, S. Li, C. Wang, J. Guo, J. Zhao, and H. Xu, Two-dimensional quantum transport in free-standing InSb nanosheets, *Nano Lett.* **19**, 561 (2019).
- [25] J. Xue, Y. Chen, D. Pan, J.-Y. Wang, J. Zhao, S. Huang, and H. Q. Xu, Gate defined quantum dot realized in a single crystalline InSb nanosheet, *Appl. Phys. Lett.* **114**, 023108 (2019).
- [26] Y. Chen, S. Huang, D. Pan, J. Xue, L. Zhang, J. Zhao, and H. Q. Xu, Strong and tunable spin-orbit interaction in a single crystalline InSb nanosheet, *npj 2D Mater. Appl.* **5**, 3 (2021).
- [27] S. Gazibegovic, G. Badawy, T. L. J. Buckers, P. Leubner, J. Shen, F. K. de Vries, S. Koelling, L. P. Kouwenhoven, M. A. Verheijen, and E. P. A. M. Bakkers, Bottom-up grown 2D InSb nanostructures, *Adv. Mater.* **31**, 1808181 (2019).
- [28] I. Verma, S. Salimian, V. Zannier, S. Heun, F. Rossi, D. Ercolani, F. Beltram, and L. Sorba, High-mobility free-standing InSb nanoflags grown on InP nanowire stems for quantum devices, *ACS Appl. Nano Mater.* **4**, 5825 (2021).
- [29] M. Rossi, G. Badawy, Z.-Y. Zhang, G. Yang, G.-A. Li, J.-Y. Shi, R. L. M. Op het Veld, S. Gazibegovic, L. Li, J. Shen *et al.*, Merging nanowires and formation dynamics of bottom-up grown InSb nanoflakes, *Adv. Funct. Mater.* **33**, 2212029 (2023).
- [30] S. Salimian, M. Carrega, I. Verma, V. Zannier, M. P. Nowak, F. Beltram, L. Sorba, and S. Heun, Gate-controlled supercurrent in ballistic InSb nanoflag Josephson junctions, *Appl. Phys. Lett.* **119**, 214004 (2021).
- [31] B. Turini, S. Salimian, M. Carrega, A. Iorio, E. Strambini, F. Giazotto, V. Zannier, L. Sorba, and S. Heun, Josephson diode effect in high-mobility InSb nanoflags, *Nano Lett.* **22**, 8502 (2022).
- [32] A. Fornieri, A. M. Whiticar, F. Setiawan, E. Portolés, A. C. C. Drachmann, A. Keselman, S. Gronin, C. Thomas, T. Wang *et al.*, Evidence of topological superconductivity in planar Josephson junctions, *Nature (London)* **569**, 89 (2019).
- [33] E. Prada, P. San-Jose, M. W. A. de Moor, A. Geresdi, E. J. H. Lee, J. Klinovaja, D. Loss, J. Nygård, R. Aguado, and L. P. Kouwenhoven, From Andreev to Majorana bound states in hybrid superconductor–semiconductor nanowires, *Nat. Rev. Phys.* **2**, 575 (2020).
- [34] T. W. Larsen, K. D. Petersson, F. Kuemmeth, T. S. Jespersen, P. Krogstrup, J. Nygård, and C. M. Marcus, Semiconductor-nanowire-Based Superconducting Qubit, *Phys. Rev. Lett.* **115**, 127001 (2015).
- [35] L. Casparis, M. R. Connolly, M. Kjaergaard, N. J. Pearson, A. Kringhøj, T. W. Larsen, F. Kuemmeth, T. Wang, C. Thomas, S. Gronin *et al.*, Superconducting gatemon qubit based on a proximitized two-dimensional electron gas, *Nat. Nanotechnol.* **13**, 915 (2018).
- [36] M. Hays, V. Fatemi, D. Bouman, J. Cerrillo, S. Diamond, K. Serniak, T. Connolly, P. Krogstrup, J. Nygård, A. Levy Yeyati *et al.*, Coherent manipulation of an Andreev spin qubit, *Science* **373**, 430 (2021).
- [37] J. Basset, M. Kuzmanović, P. Virtanen, T. T. Heikkilä, J. Estève, J. Gabelli, C. Strunk, and M. Aprili, Nonadiabatic dynamics in strongly driven diffusive Josephson junctions, *Phys. Rev. Res.* **1**, 032009(R) (2019).
- [38] G. Catelani and D. Basko, Non-equilibrium quasiparticles in superconducting circuits: Photons vs. phonons, *SciPost Phys.* **6**, 013 (2019).
- [39] M. Kjaergaard, H. J. Suominen, M. P. Nowak, A. R. Akhmerov, J. Shabani, C. J. Palmstrøm, F. Nichele, and C. M. Marcus, Transparent Semiconductor-Superconductor Interface and Induced Gap in an Epitaxial Heterostructure Josephson Junction, *Phys. Rev. Appl.* **7**, 034029 (2017).
- [40] P. Russer, Influence of microwave radiation on current-voltage characteristic of superconducting weak links, *J. Appl. Phys.* **43**, 2008 (1972).
- [41] T. F. Q. Larson, L. Zhao, E. G. Arnault, M.-T. Wei, A. Seredinski, H. Li, K. Watanabe, T. Taniguchi, F. Amet, and G. Finkelstein, Zero crossing steps and anomalous Shapiro maps in graphene Josephson junctions, *Nano Lett.* **20**, 6998 (2020).
- [42] H. Courtois, M. Meschke, J. T. Peltonen, and J. P. Pekola, Origin of Hysteresis in a Proximity Josephson Junction, *Phys. Rev. Lett.* **101**, 067002 (2008).
- [43] In our device the geometric junction capacitance is estimated \sim aF, which may not cause a noticeable hysteresis, but intrinsic capacitance effects cannot be ruled out [73–75].
- [44] I. V. Borzenets, U. C. Coskun, S. J. Jones, and G. Finkelstein, Phase Diffusion in Graphene-Based Josephson Junctions, *Phys. Rev. Lett.* **107**, 137005 (2011).
- [45] I. V. Borzenets, F. Amet, C. T. Ke, A. W. Draelos, M. T. Wei, A. Seredinski, K. Watanabe, T. Taniguchi, Y. Bomze, M. Yamamoto *et al.*, Ballistic Graphene Josephson Junctions from the Short to the Long Junction Regimes, *Phys. Rev. Lett.* **117**, 237002 (2016).
- [46] C. W. J. Beenakker, Universal Limit of Critical-Current Fluctuations in Mesoscopic Josephson Junctions, *Phys. Rev. Lett.* **67**, 3836 (1991).
- [47] We are assuming for simplicity a BCS gap [102].

- [48] P. Dubos, H. Courtois, B. Pannetier, F. K. Wilhelm, A. D. Zaikin, and G. Schön, Josephson critical current in a long mesoscopic S-N-S junction, *Phys. Rev. B* **63**, 064502 (2001).
- [49] The constant a is dependent on the ratio E_{Th}/Δ^* [48].
- [50] M. Kayyalha, M. Kargarian, A. Kazakov, I. Miotkowski, V. M. Galitski, V. M. Yakovenko, L. P. Rokhinson, and Y. P. Chen, Anomalous Low-Temperature Enhancement of Supercurrent in Topological-Insulator Nanoribbon Josephson Junctions: Evidence for Low-Energy Andreev Bound States, *Phys. Rev. Lett.* **122**, 047003 (2019).
- [51] P. Schüffelgen, D. Rosenbach, C. Li, T. W. Schmitt, M. Schleenvoigt, A. R. Jalil, S. Schmitt, J. Kölzer, M. Wang, B. Bennemann *et al.*, Selective area growth and stencil lithography for in situ fabricated quantum devices, *Nat. Nanotechnol.* **14**, 825 (2019).
- [52] V. S. Stolyarov, D. S. Yakovlev, S. N. Kozlov, O. V. Skryabina, D. S. Lvov, A. I. Gumarov, O. V. Emelyanova, P. S. Dzhumayev, I. V. Shchetinin, R. A. Hovhannisyanyan *et al.*, Josephson current mediated by ballistic topological states in $\text{Bi}_2\text{Te}_{2.3}\text{Se}_{0.7}$ single nanocrystals, *Commun. Mater.* **1**, 38 (2020).
- [53] D. Rosenbach, T. W. Schmitt, P. Schüffelgen, M. P. Stehno, C. Li, M. Schleenvoigt, A. R. Jalil, G. Mussler, E. Neumann, S. Trellenkamp *et al.*, Reappearance of first Shapiro step in narrow topological Josephson junctions, *Sci. Adv.* **7**, eabf1854 (2021).
- [54] T. W. Schmitt, B. Frohn, W. Wittl, A. R. Jalil, M. Schleenvoigt, E. Zimmermann, A. Schmidt, T. Schäpers, J. C. Cuevas, A. Brinkman *et al.*, Anomalous temperature dependence of multiple Andreev reflections in a topological insulator Josephson junction, *Supercond. Sci. Technol.* **36**, 024002 (2023).
- [55] V. Barzykin and A. M. Zagoskin, Coherent transport and nonlocality in mesoscopic SNS junctions: Anomalous magnetic interference patterns, *Superlattices Microstruct.* **25**, 797 (1999).
- [56] J. C. Cuevas and F. S. Bergeret, Magnetic Interference Patterns and Vortices in Diffusive SNS Junctions, *Phys. Rev. Lett.* **99**, 217002 (2007).
- [57] L. Angers, F. Chiodi, G. Montambaux, M. Ferrier, S. Guéron, H. Bouchiat, and J. C. Cuevas, Proximity dc squids in the long-junction limit, *Phys. Rev. B* **77**, 165408 (2008).
- [58] F. Chiodi, M. Ferrier, S. Guéron, J. C. Cuevas, G. Montambaux, F. Fortuna, A. Kasumov, and H. Bouchiat, Geometry-related magnetic interference patterns in long SNS Josephson junctions, *Phys. Rev. B* **86**, 064510 (2012).
- [59] T. J. Blom, T. W. Mechielsen, R. Fermin, M. B. S. Hesselberth, J. Aarts, and K. Lahabi, Direct-write printing of Josephson junctions in a scanning electron microscope, *ACS Nano* **15**, 322 (2021).
- [60] A. I. Gubin, K. S. Il'in, S. A. Vitusevich, M. Siegel, and N. Klein, Dependence of magnetic penetration depth on the thickness of superconducting Nb thin films, *Phys. Rev. B* **72**, 064503 (2005).
- [61] S. Shapiro, Josephson Currents in Superconducting Tunneling: The Effect of Microwaves and other Observations, *Phys. Rev. Lett.* **11**, 80 (1963).
- [62] A. D. Zaikin, Nonstationary Josephson effect and nonequilibrium properties of SNS junctions, *Sov. Phys. JETP* **57**, 910 (1983).
- [63] N. Argaman, Nonequilibrium Josephson-like effects in wide mesoscopic SNS junctions, *Superlattices Microstruct.* **25**, 861 (1999).
- [64] P. Dubos, H. Courtois, O. Buisson, and B. Pannetier, Coherent Low-Energy Charge Transport in a Diffusive S-N-S Junction, *Phys. Rev. Lett.* **87**, 206801 (2001).
- [65] M. Fuechsle, J. Bentner, D. A. Ryndyk, M. Reinwald, W. Wegscheider, and C. Strunk, Effect of Microwaves on the Current-Phase Relation of Superconductor–Normal-Metal–Superconductor Josephson Junctions, *Phys. Rev. Lett.* **102**, 127001 (2009).
- [66] B. Dassonneville, A. Murani, M. Ferrier, S. Guéron, and H. Bouchiat, Coherence-enhanced phase-dependent dissipation in long SNS Josephson junctions: Revealing Andreev bound state dynamics, *Phys. Rev. B* **97**, 184505 (2018).
- [67] K. Ueda, S. Matsuo, H. Kamata, Y. Sato, Y. Takeshige, K. Li, L. Samuelson, H. Xu, and S. Tarucha, Evidence of half-integer Shapiro steps originated from nonsinusoidal current phase relation in a short ballistic InAs nanowire Josephson junction, *Phys. Rev. Res.* **2**, 033435 (2020).
- [68] J. Pfeiffer, M. Kemmler, D. Koelle, R. Kleiner, E. Goldobin, M. Weides, A. K. Feofanov, J. Lisenfeld, and A. V. Ustinov, Static and dynamic properties of 0 , π , and $0-\pi$ ferromagnetic Josephson tunnel junctions, *Phys. Rev. B* **77**, 214506 (2008).
- [69] M. J. A. Stoutimore, A. N. Rossolenko, V. V. Bolginov, V. A. Oboznov, A. Y. Rusanov, D. S. Baranov, N. Pugach, S. M. Frolov, V. V. Ryazanov, and D. J. Van Harlingen, Second-Harmonic Current-Phase Relation in Josephson Junctions with Ferromagnetic Barriers, *Phys. Rev. Lett.* **121**, 177702 (2018).
- [70] O. O. Shvetsov, A. Kononov, A. V. Timonina, N. N. Kolesnikov, and E. V. Deviatov, Subharmonic Shapiro steps in the a.c. Josephson effect for a three-dimensional Weyl semimetal WTe_2 , *EPL (Europhys. Lett.)* **124**, 47003 (2018).
- [71] C. J. Trimble, M. T. Wei, N. F. Q. Yuan, S. S. Kalantre, P. Liu, H.-J. Han, M.-G. Han, Y. Zhu, J. J. Cha, L. Fu, and J. R. Williams, Josephson detection of time-reversal symmetry broken superconductivity in SnTe nanowires, *npj Quantum Mater.* **6**, 61 (2021).
- [72] U. Eckern, G. Schön, and V. Ambegaokar, Quantum dynamics of a superconducting tunnel junction, *Phys. Rev. B* **30**, 6419 (1984).
- [73] D. S. Antonenko and M. A. Skvortsov, Quantum decay of the supercurrent and intrinsic capacitance of Josephson junctions beyond the tunnel limit, *Phys. Rev. B* **92**, 214513 (2015).
- [74] D. Massarotti, N. Banerjee, R. Caruso, G. Rotoli, M. G. Blamire, and F. Tafuri, Electrodynamics of Josephson junctions containing strong ferromagnets, *Phys. Rev. B* **98**, 144516 (2018).
- [75] R. Fischer, J. Picó-Cortés, W. Himmler, G. Platero, M. Grifoni, D. A. Kozlov, N. N. Mikhailov, S. A. Dvoretzky, C. Strunk, and D. Weiss, 4π -periodic supercurrent tuned by an axial magnetic flux in topological insulator nanowires, *Phys. Rev. Res.* **4**, 013087 (2022).
- [76] C. A. Hamilton and E. Johnson, Analog computer studies of subharmonic steps in superconducting weak links, *Phys. Lett. A* **41**, 393 (1972).
- [77] T. F. Q. Larson, L. Zhao, E. G. Arnault, M.-T. Wei, A. Seredinski, H. Li, K. Watanabe, T. Tanaguchi, F. Amet, and G. Finkelstein, Noise-induced stabilization of dynamical states

- in a non-Markovian system, [arXiv:2212.13952](#) [cond-mat] (2022).
- [78] K. H. Lee, D. Stroud, and J. S. Chung, Calculation of Giant Fractional Shapiro Steps in Josephson-Junction Arrays, *Phys. Rev. Lett.* **64**, 962 (1990).
- [79] H. C. Lee, R. S. Newrock, D. B. Mast, S. E. Hebboul, J. C. Garland, and C. J. Lobb, Subharmonic Shapiro steps in Josephson-junction arrays, *Phys. Rev. B* **44**, 921 (1991).
- [80] E. Heinz and P. Seidel, Microwave-induced steps in Josephson junctions, DC-SQUIDS and parallel arrays, *J. Low Temp. Phys.* **106**, 233 (1997).
- [81] A. Valizadeh, M. R. Kollahchi, and J. P. Straley, Fractional Shapiro steps in a triangular single-plaquette Josephson-junction array, *Phys. Rev. B* **76**, 214511 (2007).
- [82] R. Panghotra, B. Raes, C. C. de Souza Silva, I. Cools, W. Keijers, J. E. Scheerder, V. V. Moshchalkov, and J. Van de Vondel, Giant fractional Shapiro steps in anisotropic Josephson junction arrays, *Commun. Phys.* **3**, 1 (2020).
- [83] F. Amet, S. Idris, A. McConnell, B. Opatosky, and E. Arnault, Phase dynamics in an AC-driven multiterminal Josephson junction analog, *Phys. Rev. B* **106**, 174509 (2022).
- [84] C. Vanneste, C. C. Chi, W. J. Gallagher, A. W. Kleinsasser, S. I. Raider, and R. L. Sandstrom, Shapiro steps on current-voltage curves of dc SQUIDS, *J. Appl. Phys.* **64**, 242 (1988).
- [85] E. A. Early, A. F. Clark, and C. J. Lobb, Physical basis for half-integral Shapiro steps in a DC SQUID, *Physica C: Superconductivity* **245**, 308 (1995).
- [86] E. A. Early, A. F. Clark, and K. Char, Half-integral constant voltage steps in high- T_c grain boundary junctions, *Appl. Phys. Lett.* **62**, 3357 (1993).
- [87] D. Terpstra, R. P. J. IJsselsteijn, and H. Rogalla, Subharmonic Shapiro steps in high- T_c Josephson junctions, *Appl. Phys. Lett.* **66**, 2286 (1995).
- [88] L. Ku, H. Cho, and S. Wang, The origin of the half-integral constant voltage steps in high- T_c grain-boundary junction, *Physica C: Superconductivity* **243**, 187 (1995).
- [89] H. C. Yang, L. C. Ku, H. M. Cho, J. H. Lu, and H. E. Horng, Observation of half-integer Shapiro steps in step-edge $\text{YBa}_2\text{Cu}_3\text{O}_y$ Josephson junctions, *Physica C: Superconductivity* **235–240**, 3341 (1994).
- [90] H. Kroemer, Quasiparticle dynamics in ballistic weak links under weak voltage bias: An elementary treatment, *Superlattices Microstruct.* **25**, 877 (1999).
- [91] K. Biedermann, A. Chrestin, T. Matsuyama, and U. Merkt, Ac Josephson effects in Nb/InAs/Nb junctions with integrated resonators, *Phys. Rev. B* **63**, 144512 (2001).
- [92] J. J. A. Baselmans, T. T. Heikkilä, B. J. van Wees, and T. M. Klapwijk, Direct Observation of the Transition from the Conventional Superconducting State to the π State in a Controllable Josephson Junction, *Phys. Rev. Lett.* **89**, 207002 (2002).
- [93] J. C. Cuevas, J. Heurich, A. Martín-Rodero, A. Levy Yeyati, and G. Schön, Subharmonic Shapiro Steps and Assisted Tunneling in Superconducting Point Contacts, *Phys. Rev. Lett.* **88**, 157001 (2002).
- [94] A. Jacobs and R. Kümmel, Andreev scattering, Zener tunneling, and anomalous ac Josephson effect in near-ballistic quasi-two-dimensional weak links, *Phys. Rev. B* **71**, 184504 (2005).
- [95] P. Virtanen, T. T. Heikkilä, F. S. Bergeret, and J. C. Cuevas, Theory of Microwave-Assisted Supercurrent in Diffusive SNS Junctions, *Phys. Rev. Lett.* **104**, 247003 (2010).
- [96] F. S. Bergeret, P. Virtanen, A. Ozaeta, T. T. Heikkilä, and J. C. Cuevas, Supercurrent and Andreev bound state dynamics in superconducting quantum point contacts under microwave irradiation, *Phys. Rev. B* **84**, 054504 (2011).
- [97] D. Z. Haxell, M. Coraiola, D. Sabonis, M. Hinderling, S. C. ten Kate, E. Cheah, F. Krizek, R. Schott, W. Wegscheider, W. Belzig *et al.*, Microwave-induced conductance replicas in hybrid Josephson junctions without Floquet-Andreev states, [arXiv:2212.03554](#) [cond-mat] (2022).
- [98] Z. Dou, T. Wakamura, P. Virtanen, N.-J. Wu, R. Deblock, S. Autier-Laurent, K. Watanabe, T. Taniguchi, S. Guéron, H. Bouchiat, and M. Ferrier, Microwave photoassisted dissipation and supercurrent of a phase-biased graphene-superconductor ring, *Phys. Rev. Res.* **3**, L032009 (2021).
- [99] K. Flensberg, J. B. Hansen, and M. Octavio, Subharmonic energy-gap structure in superconducting weak links, *Phys. Rev. B* **38**, 8707 (1988).
- [100] B. A. Aminov, A. A. Golubov, and M. Yu. Kupriyanov, Quasiparticle current in ballistic constrictions with finite transparencies of interfaces, *Phys. Rev. B* **53**, 365 (1996).
- [101] J. C. Cuevas and A. Levy Yeyati, Subharmonic gap structure in short ballistic graphene junctions, *Phys. Rev. B* **74**, 180501 (2006).
- [102] B. Möhlschlegel, Die thermodynamischen Funktionen des Supraleiters, *Z. Phys.* **155**, 313 (1959).